



# 1 New method to determine black carbon mass size distribution

2 Weilun Zhao<sup>1</sup>, Gang Zhao<sup>2</sup>, Ying Li<sup>3,4</sup>, Song Guo<sup>2</sup>, Nan Ma<sup>5</sup>, Lizi Tang<sup>2</sup>, Zirui Zhang<sup>2</sup>, Chunsheng Zhao<sup>1</sup>

3 <sup>1</sup>Department of Atmospheric and Oceanic Sciences, School of Physics, Peking University, Beijing 100871, China

4 <sup>2</sup>State Key Joint Laboratory of Environmental Simulation and Pollution Control, College of Environmental Sciences and  
5 Engineering, Peking University, Beijing 100871, China

6 <sup>3</sup>Department of Ocean Science and Engineering, Southern University of Science and Technology, Shenzhen 518055, China

7 <sup>4</sup>Southern Marine Science and Engineering Guangdong Laboratory, Guangzhou 511458, China

8 <sup>5</sup>Institute for Environmental and Climate Research, Jinan University, Guangzhou 511443, China

9 *Correspondence to:* Chunsheng Zhao ([zcs@pku.edu.cn](mailto:zcs@pku.edu.cn))

10 **Abstract.** Black carbon (BC) is an important atmospheric component with strong light absorption. Many attempts have been made  
11 to measure BC mass size distribution (BCMSD) for its significant impact on climate and public health. Larger-coverage BCMSD,  
12 ranging from upper submicron to larger than 1  $\mu\text{m}$ , contributes to substantial proportion of BC absorption. However, current time  
13 resolution of larger-coverage BCMSD measurement was limited to 1 day, which was insufficient to characterize variation of larger-  
14 coverage BCMSD. In this study, a new method to determine BCMSD was proposed from size-resolved absorption coefficient  
15 measured by an aerodynamic aerosol classifier in tandem with an aethalometer. The proposed method could measure larger-coverage  
16 BCMSD with time resolution as high as 1 hour and was validated by comparing the measurement results with that measured by a  
17 differential mobility analyzer in tandem with a single particle soot photometer (DMA – SP2) for particle size larger than 300 nm  
18 during a field measurement in Yangtze River Delta. Bulk BC mass concentration ( $m_{\text{BC,bulk}}$ ) by DMA – SP2 was underestimated by  
19 33 % compared to that by this method because of the limited size range of measurement for DMA – SP2. Uncertainty analysis of  
20 this method was performed with respect to mass absorption cross-section (MAC), transfer function inversion, number fraction of  
21 BC-containing particle and instrumental noise. The results indicated that MAC was the main uncertainty source, leading to  $m_{\text{BC,bulk}}$   
22 varied from – 20 % to 28 %. With the advantage of wide size coverage up to 1.5  $\mu\text{m}$ , high time resolution, easy operation and low  
23 cost, this method is expected to have wide applications in field measurement for better estimating radiative properties and climate  
24 effects of BC.

## 25 1 Introduction

26 Atmospheric black carbon (BC) is emitted through incomplete combustion of carbon-based fuels (Bond, 2001), such as biomass  
27 burning and fossil fuel combustion (Bond et al., 2004). BC warms atmosphere and is considered the third important light absorber  
28 in the climate system after  $\text{CO}_2$  and  $\text{CH}_4$  (Bond et al., 2013). BC can induce the respiratory and cardiovascular disease through  
29 inhalation (Highwood and Kinnersley, 2006). Plenty of studies have been devoted to BC for its significant impact on the climate  
30 and public health.

31 Bulk BC mass concentration ( $m_{\text{BC,bulk}}$ ) is one of the essential parameters for modeling because radiative transfer models calculate



32 BC absorption from  $m_{\text{BC,bulk}}$  (Bond et al., 2013). A great deal of research has been dedicated to  $m_{\text{BC,bulk}}$  measurement for both  
33 model assimilation and environmental monitoring (Castagna et al., 2019; Helin et al., 2018; Ran et al., 2016). A recent study indicated  
34 that the radiative effect of BC was extremely sensitive to its particle size (Matsui et al., 2018). Zhao et al. (2019) further revealed  
35 that the variation of BC mass size distribution (BCMSD), namely size-resolved BC mass concentration ( $m_{\text{BC,size-resolved}}$ ), led to  
36 substantial changes in the radiative effect of BC based on field measurement, highlighting the importance of BCMSD on modeling  
37 the radiative effect of BC rather than simply  $m_{\text{BC,bulk}}$ . The size of BC affects the deposition rate of BC to the lung (Highwood and  
38 Kinnersley, 2006), indicating that BCMSD is closely related to health. In the ambient environment, BCMSD is influenced by  
39 emission sources. For instance, BCMSD of fossil fuel combustion differs obviously from that of biomass burning (Schwarz et al.,  
40 2008), implying that BCMSD is one of the characteristics of emission source. The temporal variation of BCMSD can reflect the  
41 atmospheric aging of BC, during which BC undergoes remarkable change in size, accompanied by dramatical variation of BC optical  
42 properties (Zhang et al., 2008). Therefore, reliable measurement and understanding of BCMSD are highly necessary for estimating  
43 the impact of BC on both the earth energy budget and public health (Moosmuller et al., 2009).

44 Quite a few efforts were made to measure BCMSD. The single-particle soot photometer (SP2) was developed using laser-induced  
45 incandescence (Schwarz et al., 2006), which measured BCMSD on a single-particle level. The soot particle aerosol mass  
46 spectrometer (SP-AMS) combined laser-induced incandescence and mass spectroscopy, which could determine not only BCMSD  
47 but also the chemical composition of BC-containing particles (Onasch et al., 2012). The SP2 and SP-AMS techniques were  
48 characterized by high time resolution and high accuracy, but high cost and complicated maintenance, as a result, not widely applied  
49 for routine measurement. A more convenient solution was required for wider and better characterization of BCMSD in different  
50 regions and emission sources. BCMSD could be sampled by multi-stage cascade impactor (Viidanoja et al., 2002) combined with  
51 off-line analysis, such as thermo/optical organic carbon/elemental carbon method (Chow et al., 2001). BCMSD sampled by multi-  
52 stage cascade impactor had wide size coverage, but low time resolution, usually from 24 hours (Soto-Garcia et al., 2011) to 48 hours  
53 (Guo, 2015), which was too low to resolve aging of BC. Differential mobility analyzer (DMA) in tandem with filter-based instrument  
54 (Hansen et al., 1984), for instance, micro-aethalometer (MA) (Ning et al., 2013) and particle soot absorption photometer (PSAP)  
55 (Tunved et al., 2021), was used to determine BCMSD with higher time resolution up to 2 hours (Zhao et al., 2021). However, the  
56 multiple-charge correction and low flow rate of DMA imposed restrictions on the accuracy of the measured BCMSD. The measured  
57 size range of DMA was limited to less than about 700 nm, resulting in incomplete measured BCMSD. Current measurement of  
58 larger-coverage BCMSD ranging from upper submicron to larger than 1  $\mu\text{m}$  was limited in time resolution. Characteristics of larger-  
59 coverage BCMSD during atmospheric aging was still unclear. Therefore, it was imperative to measure larger-coverage BCMSD  
60 with higher time resolution.

61 In this study, a new method to determine BCMSD was proposed using size-resolved absorption coefficient ( $\sigma_{\text{ab,size-resolved}}$ )  
62 measured by an aerodynamic aerosol classifier (AAC, Cambustion, UK, Tavakoli and Olfert (2013)) in tandem with an aethalometer  
63 (model AE33, Magee, USA, Drinovec et al. (2015)), combined with size-resolved number concentration ( $N_{\text{size-resolved}}$ ),



64 simultaneously measured by scanning mobility particle sizer (SMPS, TSI, USA) and an aerodynamic particle sizer (APS, TSI, USA).  
65 The proposed method for determining BCMSD overcame the disadvantages and weighed the advantages of the above-mentioned  
66 methods, characterized by high cost-effectiveness, easy and convenient maintenance, high time resolution to 1 hour, and wide size  
67 range to up to 1.5  $\mu\text{m}$ . The proposed method was validated in a field measurement in the Yangtze River Delta and the uncertainty  
68 study was carried out based on the measured data.

## 69 2 Experimental setup

### 70 2.1 Instrumental setup

71 Figure 1 illustrated the instrumental setup developed in this study, which could be split into two parts, namely the measurement  
72 setup and the validation setup. Ambient aerosol particles were dried to relative humidity (RH) less than 30 % beforehand. For the  
73 measurement setup, AAC in tandem with AE33 (AAC – AE33) measured  $\sigma_{\text{ab, size-resolved}}$  at a flow rate of 3 L  $\text{min}^{-1}$ . Since BCMSD  
74 of larger size coverage was mainly focused in this study, AAC was set to scan 12 logarithmically spaced particle sizes ( $D_p$ ) from  
75 200 nm to 1500 nm. Each size was scanned for 5 minutes and 1 hour was required for a complete cycle. It should be noted that  $D_p$   
76 was aerodynamic size in this study. Mobility size related to DMA was converted to aerodynamic size assuming an effective density  
77 of 1.3 g  $\text{cm}^{-3}$  (Zhao et al., 2019; DeCarlo et al., 2005). AE33 measured absorption coefficient ( $\sigma_{\text{ab}}$ ) at 7 wavelengths from 370 nm  
78 to 950 nm (Drinovec et al., 2015), at which 880 nm was adopted in this study because BC dominated particle absorption at 880 nm  
79 (Ramachandran and Rajesh, 2007). SMPS and APS measured  $N_{\text{size-resolved}}$  for  $D_p$  less than and greater than about 800 nm at a  
80 flow rate of 0.3 L  $\text{min}^{-1}$  and 5 L  $\text{min}^{-1}$ , respectively.

81 For validation system, the tandem array of Neutralizer, DMA and SP2 (DMA – SP2) measured BCMSD ( $\text{BCMSD}_{\text{DMA-SP2}}$ ) at a  
82 flow rate of 0.12 L  $\text{min}^{-1}$  for purpose of comparing with BCMSD determined by the proposed method ( $\text{BCMSD}_{\text{AAC-AE33}}$ ). The lower  
83 detection limit of  $D_p$  for DMA – SP2 was about 200 nm (Zhao et al., 2020a). Therefore, lower  $D_p$  limit for both  $\text{BCMSD}_{\text{DMA-SP2}}$   
84 and  $\text{BCMSD}_{\text{AAC-AE33}}$  was set as 200 nm in this study. Another AE33 measured bulk absorption coefficient ( $\sigma_{\text{ab, bulk}}$ ) simultaneously  
85 at a flow rate of 2 L  $\text{min}^{-1}$  for closure study with  $\sigma_{\text{ab, size-resolved}}$ .

### 86 2.2 Aethalometer model AE33

87 The principle of obtaining  $\sigma_{\text{ab}}$  was well developed for aethalometer (Hansen et al., 1984) and described here in brief. Ambient  
88 aerosol particles were drawn into an aethalometer at a flow rate  $F$  and collected on an area  $S$  of a filter. A light source illuminated  
89 the filter. The transmitted light signal was denoted as  $I$  ( $I_0$ ) for the light which passed through the particle-laden (particle-free) part  
90 of the filter. Light attenuation was defined as

$$91 \text{ATN} = -100 \cdot \ln\left(\frac{I}{I_0}\right). \quad (1)$$

92 ATN increased with decreasing  $I$  as aerosol particles were loaded on the filter continuously. Therefore, ATN reflected aerosol  
93 loading on the filter. If ATN increased  $\Delta\text{ATN}$  during time interval  $\Delta t$ , then attenuation coefficient was defined as

$$94 \sigma_{\text{ATN}} = \frac{S}{100 \cdot F} \cdot \frac{\Delta\text{ATN}}{\Delta t}. \quad (2)$$



95 The light attenuation was caused by not only particle absorption, but also scattering by particle and filter matrix. A scattering  
96 parameter  $C$  was introduced to extract  $\sigma_{ab}$  from  $\sigma_{ATN}$ :

$$97 \quad \sigma_{ab} = \frac{\sigma_{ATN}}{C}, \quad (3)$$

98 where  $C$  was set as 2.9 (Zhao et al., 2020b) in this study. Nonlinearity, termed loading effect, became more and more significant  
99 with increasing aerosol loading, namely for the same increase in aerosol loading, the corresponding increase in ATN was smaller  
100 for heavier aerosol loading. The “dual-spot” technique (Drinovec et al., 2015) was proposed to correct the loading effect for AE33  
101 and was used in this study. The  $\sigma_{ab}$  measured by AE33 at given a particle size selected by AAC was termed binned  $\sigma_{ab}$  ( $\sigma_{ab,binned}$ )  
102 in this study to differentiate from  $\sigma_{ab,bulk}$ .

### 103 2.3 Aerodynamic aerosol classifier

104 The principle of AAC was illustrated detailedly by Tavakoli and Olfert (2013) and was introduced here concisely. The setup of  
105 AAC could be simplified to two coaxial cylinders, where the inner radius, outer radius and length was denoted as  $r_i$ ,  $r_o$  and  $L$ .  
106 Polydisperse particles flowed into the space between the inner cylinder and outer cylinder from one end of the inner cylinder at a  
107 flow rate of  $Q_{sample}$ . Meanwhile, Particle free sheath flow streamed in the space between the inner cylinder and outer cylinder in the  
108 direction of the axis of the coaxial cylinders at a flow rate of  $Q_{sheath}$ . The sheath flow carried the particles along the coaxial cylinders.  
109 At the same time, the two coaxial cylinders rotated with respect to their axis at a rotational speed of  $\omega$ . Therefore, the particles was  
110 migrated outwards across the sheath flow by the centrifugal force acting on them. Relaxation time ( $\tau$ ) was defined as

$$111 \quad \tau = \frac{C_c(D_p)\rho_0 D_p^2}{18\mu}, \quad (4)$$

112 where  $C_c(D_p)$  was the Cunningham slip correction factor as a function of  $D_p$  (Kim et al., 2005),  $\rho_0 = 1 \text{ g cm}^{-3}$  was the reference  
113 density and  $\mu$  was the gas viscosity. It could be seen that  $\tau$  was directly related to  $D_p$ . Dynamic analysis proved that only particles  
114 with certain relaxation time  $\tau$ , and hence certain  $D_p$ , could migrate to another end of outer cylinder and emerge as monodisperse  
115 flow.  $\tau$  was related to parameters of AAC by

$$116 \quad \tau = \frac{2Q_{sh}}{\pi\omega^2(r_i+r_o)^2L}. \quad (5)$$

117 Therefore, by changing  $\omega$  and  $Q_{sh}$ , monodisperse particles of desired  $D_p$  could be selected by AAC. Unlike DMA, particles did  
118 not need to be charged before entering AAC. Consequently, the transmission efficiency ( $\lambda_n$ ) of AAC about 4 times higher than that  
119 of DMA and multi-charge correction was not required for data measured by the instrument downstream AAC (Johnson et al., 2018).

## 120 2.4 Method

### 121 2.4.1 Deriving size-resolved absorption coefficient from binned absorption coefficient

122 Tavakoli and Olfert (2013) formulated the ideal theoretical model for AAC transfer function inversion, which was adopted by this  
123 study to derive  $\sigma_{ab,size-resolved}$  from  $\sigma_{ab,binned}$  and presented here in short. The  $\sigma_{ab,size-resolved}$  was given by

$$124 \quad \sigma_{ab,size-resolved} = \frac{d\sigma_{ab}}{d\log D_p} = \frac{\ln(10)}{d\log D_p \cdot \beta^*} \cdot \sigma_{ab,binned}, \quad (6)$$



125 where  $\beta^*$  was related to the ratio of  $Q_{\text{sheath}}$  to  $Q_{\text{sample}}$ ,  $R_t = \frac{Q_{\text{sheath}}}{Q_{\text{sample}}} = \frac{1}{\beta^*}$ , through

$$126 \quad \beta^* = \left(1 + \frac{1}{\beta}\right) \ln(1 + \beta) - \left(1 - \frac{1}{\beta}\right) \ln(1 - \beta). \quad (7)$$

127 Johnson et al. (2018) corrected the ideal inversion formula (6) to take particle loss and spectral broadening into account by replacing

128  $\beta^*$  with a nonideal  $\beta_{\text{NI}}^*$ :

$$129 \quad \beta_{\text{NI}}^* = \lambda_{\Omega} \mu_{\Omega} \left[ \ln \left( \frac{1 - \beta / \mu_{\Omega}}{1 + \beta / \mu_{\Omega}} \right) + \frac{\mu_{\Omega}}{\beta} \ln \left( 1 - \left( \frac{\mu_{\Omega}}{\beta} \right)^2 \right) \right], \quad (8)$$

130 where  $\mu_{\Omega}$  was the spectral broadening factor. Both  $\lambda_{\Omega}$  and  $\mu_{\Omega}$  were dependent on  $D_p$  as well as flow, and discussed in detail in  
 131 Sect. 4.2.

#### 132 **2.4.2 Deriving black carbon mass size distribution from size-resolved absorption coefficient**

133  $\sigma_{\text{ab,size-resolved}}$  could be converted to  $\text{BCMSD}_{\text{AAC-AE33}}$  through mass absorption cross-section (MAC) (Bond and Bergstrom,  
 134 2006), which was assumed a fixed value of  $7.77 \text{ m}^2/\text{g}$  for AE33 (Drinovec et al., 2015). However, both field measurement (Bond  
 135 and Bergstrom, 2006) and model study (Zhao et al., 2021) manifested that MAC varied significantly. A fixed MAC led to uncertainty  
 136 in derived  $\text{BCMSD}_{\text{AAC-AE33}}$ . In this study, MAC was variable based on method proposed by Zhao et al. (2021) for more accurate  
 137  $\text{BCMSD}_{\text{AAC-AE33}}$  estimation. Briefly, a 2-dimensional lookup table of MAC with respect to  $D_p$  and BC core diameter ( $D_c$ ) was  
 138 simulated (MAC( $D_p, D_c$ )) by Mie theory assuming a core-shell geometry. At a given size bin centered at  $D_p$ , the corresponding  $\sigma_{\text{ab}}$   
 139 and number concentration ( $N$ ) at the size bin, denoted as  $\sigma_{\text{ab}}(D_p)$  and  $N(D_p)$ , could be derived by  $\sigma_{\text{ab,size-resolved}}$  and  
 140  $N_{\text{size-resolved}}$ :

$$141 \quad \sigma_{\text{ab}}(D_p) = \sigma_{\text{ab,size-resolved}}(D_p) \cdot \Delta \log D_p, \quad (9)$$

$$142 \quad N(D_p) = N_{\text{size-resolved}}(D_p) \cdot \Delta \log D_p, \quad (10)$$

143 where  $\Delta \log D_p$  was the logarithmic bin width of the size bin. The number concentration of BC-containing particle  $N_{\text{BC}}(D_p)$  at  
 144 the size bin was determined by

$$145 \quad N_{\text{BC}}(D_p) = N(D_p) \cdot f_{\text{BC}}, \quad (11)$$

146 where  $f_{\text{BC}}$  was the number fraction of BC-containing particle, which was assumed as a fixed value in this study and the uncertainty  
 147 of the fixed- $f_{\text{BC}}$  assumption was discussed in Sect. 4.3. An optimal  $D_c$  was found so that calculated  $\sigma_{\text{ab}}$  at the size bin, denoted  
 148 as  $\sigma_{\text{ab,calc}}(D_p)$ , matched  $\sigma_{\text{ab}}(D_p)$ :

$$149 \quad \sigma_{\text{ab,calc}}(D_p, D_c) = \rho_{\text{BC}} \frac{\pi}{6} D_c^3 \cdot \text{MAC}(D_p, D_c) \cdot N_{\text{BC}}(D_p) = \sigma_{\text{ab}}(D_p), \quad (12)$$

150 where  $\rho_{\text{BC}}$  was the density of BC, and set as  $1.8 \text{ g cm}^{-3}$  (Bond and Bergstrom, 2006), consistent with the  $\rho_{\text{BC}}$  assumption when  
 151 deriving  $\text{BCMSD}_{\text{DMA-SP2}}$ . BC mass concentration ( $m_{\text{BC}}$ ) at the size bin, denoted as  $m_{\text{BC}}(D_p)$ , could be determined by

$$152 \quad m_{\text{BC}}(D_p) = \frac{\sigma_{\text{ab}}(D_p)}{\text{MAC}(D_p, D_c)}, \quad (13)$$

153 then the BCMSD at  $D_p$ , denoted by  $\text{BCMSD}(D_p)$ , could be determined by

$$154 \quad \text{BCMSD}(D_p) = \frac{m_{\text{BC}}(D_p)}{\Delta \log D_p}. \quad (14)$$



## 155 2.5 Field measurement

156 The proposed method was applied to a field measurement in Changzhou, Jiangsu Province, China (119°36'E, 31°43'N), located  
157 in the Yangtze River Delta, from May 17<sup>th</sup> to June 3<sup>rd</sup> in 2021. Changzhou was between two megacities, about 187 km to the  
158 northwest of Shanghai and about 82 km to the southeast of Nanjing, as shown in Fig. S1a. The area between the Shanghai and  
159 Nanjing underwent serious environmental pollution in the past few decades with the development of industrialization and  
160 urbanization. As shown in Fig. S1b, the pollution condition of Changzhou was overall representative of the regional background  
161 pollution in the Yangtze River Delta.

## 162 3 Results and discussion

163 Figure 2 presented the time series of the measurement results. There were 4 pollution episodes during the measurement period:  
164 from May 18<sup>th</sup> to May 19<sup>th</sup>, from May 21<sup>st</sup> to May 22<sup>nd</sup>, from May 24<sup>th</sup> to May 26<sup>th</sup>, and from May 29<sup>th</sup> to May 31<sup>st</sup>. Both  
165 BCMSD<sub>AAC-AE33</sub> (Fig. 2b) and BCMSD<sub>DMA-SP2</sub> (Fig. 2c) recorded the 4 pollution episodes simultaneously with higher BCMSD  
166 values than clean episodes. BCMSD<sub>AAC-AE33</sub> and BCMSD<sub>DMA-SP2</sub> were both integrated from 200 nm to 720 nm, which was the  
167  $D_p$  range of measurement for DMA – SP2, and the results were denoted as  $m_{BC,bulk,AAC-AE33,part}$  and  $m_{BC,bulk,DMA-SP2}$ ,  
168 respectively. As shown in Fig. 2a,  $m_{BC,bulk,AAC-AE33,part}$  compared well with  $m_{BC,bulk,DMA-SP2}$  with determination coefficient  
169 ( $R^2$ ), slope ( $b_1$ ), and intercept ( $b_0$ ) of 0.8 (accurate to one decimal place), 1.0 and 0.1  $\mu\text{g m}^{-3}$  (Fig. S2), indicating the proposed  
170 method was capable of capturing the variation of  $m_{BC,bulk}$ . The mean  $m_{BC,bulk,AAC-AE33,part}$  and  $m_{BC,bulk,DMA-SP2}$  were  $0.7 \pm$   
171  $0.4 \mu\text{g m}^{-3}$  and  $0.6 \pm 0.3 \mu\text{g m}^{-3}$ , indicating  $m_{BC,bulk,AAC-AE33,part}$  was overall 0.1  $\mu\text{g m}^{-3}$  higher than  $m_{BC,bulk,DMA-SP2}$ ,  
172 consistent with  $b_1$  of 0.1  $\mu\text{g m}^{-3}$ . The reason for overall discrepancy of 0.1  $\mu\text{g m}^{-3}$  in  $m_{BC,bulk}$  might be that DMA – SP2 could  
173 not detect BC with  $D_c$  less than about 100 nm (Zhao et al., 2020a), resulting in an underestimated  $m_{BC,bulk,DMA-SP2}$ .  
174 BCMSD<sub>AAC-AE33</sub> was also integrated from 200 nm to 1500 nm, which was the  $D_p$  range of measurement for DMA – SP2, and the  
175 result was denoted as  $m_{BC,bulk,AAC-AE33}$ .  $R^2$  decreased to 0.7,  $b_1$  and  $b_0$  increased to 1.2 and 0.2  $\mu\text{g m}^{-3}$  between  
176  $m_{BC,bulk,AAC-AE33}$  and  $m_{BC,bulk,DMA-SP2}$ . The mean  $m_{BC,bulk,AAC-AE33}$  was  $0.9 \pm 0.5 \mu\text{g m}^{-3}$ ,  $\sim 0.2 \mu\text{g m}^{-3}$  higher than  
177  $m_{BC,bulk,AAC-AE33,part}$ , indicating that DMA – SP2 overall underestimated  $m_{BC,bulk}$  for  $\sim 0.2 \mu\text{g m}^{-3}$  ( $\sim 33\%$ ) in this field  
178 measurement considering that DMA – SP2 could not measure BCMSD larger than about 720 nm. The decrease in  $R^2$  indicated the  
179 BCMSD of larger  $D_p$  contained more sophisticated structure. Therefore, it was highly necessary to measure BCMSD with wider  
180  $D_p$  range for better estimation of  $m_{BC,bulk}$ .

181 Figure 3 exhibited the mean BCMSD<sub>AAC-AE33</sub> ( $\overline{BCMSD}_{AAC-AE33}$ ) and mean BCMSD<sub>DMA-SP2</sub> ( $\overline{BCMSD}_{DMA-SP2}$ ) during the  
182 field measurement. It could be seen that when  $D_p$  was less than about 300 nm,  $\overline{BCMSD}_{AAC-AE33}$  was higher than  $\overline{BCMSD}_{DMA-SP2}$ .  
183 The higher  $\overline{BCMSD}_{AAC-AE33}$  may be due to particle diffusion at small  $D_p$  which was not well corrected by (7) and underestimated  
184 MAC. When  $D_p$  was greater than 300 nm and less than about 700 nm,  $\overline{BCMSD}_{AAC-AE33}$  was overall consistent with  
185  $\overline{BCMSD}_{DMA-SP2}$ . When  $D_p$  was larger than 700 nm, where DMA – SP2 could not measure,  $\overline{BCMSD}_{AAC-AE33}$  decreased with  
186 increasing  $D_p$  when  $D_p$  less than about 870 nm, and increased with increasing  $D_p$  when  $D_p$  was larger than 870 nm. In the study



187 by Yu et al. (2010), three modes of BCMSD were identified: the mode peaked at about 400 nm, 1000 nm and 5000 nm, which were  
188 termed as condensation mode, droplet mode and coarse mode, respectively. Following the nomenclature proposed by Yu et al. (2010),  
189 the increasing (decreasing)  $\overline{\text{BCMSD}}_{\text{AAC-AE33}}$  with increasing  $D_p$  for  $D_p$  larger (less) than 870 nm signified the lower (upper) end  
190 of droplet mode (condensation mode). However,  $\overline{\text{BCMSD}}_{\text{DMA-SP2}}$  only identified condensation mode, which clearly highlighted  
191 the necessity to measure BCMSD of wider  $D_p$  range for better characterization of BCMSD. Both the proposed method and DMA  
192 – SP2 showed that the temporal variation of BCMSD, expressed as standard deviation (std) of BCMSD in Fig. 3, was as large as  
193  $\overline{\text{BCMSD}}$ , reflecting the complex mechanism in the variability of BCMSD.

#### 194 4 Uncertainty analysis

195 Uncertainty analysis was performed with respect to the MAC lookup table, transfer function inversion from  $\sigma_{\text{ab,binned}}$  to  
196  $\sigma_{\text{ab,size-resolved}}$ ,  $f_{\text{BC}}$  and instrumental noise, respectively. The resulting uncertainty to  $\text{BCMSD}_{\text{AAC-AE33}}$  was illustrated in Fig. 4  
197 and to  $m_{\text{BC,bulk}}$  was shown in table 1. It could be seen from Fig. 4 that the boundary between condensation mode and droplet mode  
198 was distinct no matter how the uncertainty source disturbed  $\text{BCMSD}_{\text{AAC-AE33}}$ .

#### 199 4.1 Uncertainty from mass absorption cross-section

200 According to Zhao et al. (2021), the variation in refractive index (RI) dominated the uncertainty of the MAC lookup table.  
201 Therefore, the uncertainty from the MAC lookup table was analyzed with respect to RI. The real part of RI (Re[RI]) was reported  
202 to vary from 1.5 to 2.0 in general (Liu et al., 2018) and the imaginary part of RI (Im[RI]) ranged from 0.5 to 1.1 commonly (Bond  
203 and Bergstrom, 2006). Hence, Re[RI] (Im[RI]) was changed from 1.5 (0.5) to 2.0 (1.1) with step increase of 0.01, the resulting mean  
204 MAC ( $\overline{\text{MAC}}$ ) was the MAC lookup table used in this study (Fig. S3a) and the resulting std divided by the  $\overline{\text{MAC}}$  was considered as  
205 the uncertainty of the MAC lookup table (Fig. S3b). As shown in Fig. S2b, when  $D_c$  was larger than about 400 nm, the uncertainty  
206 was less than 10% and influenced by both  $D_p$  and  $D_c$ . However, when  $D_c$  was less than 400 nm, the uncertainty increased rapidly  
207 with decreasing  $D_c$  and was dominated by  $D_c$ . The uncertainty increased to larger than 23 % when  $D_c$  was less than about 100  
208 nm. When  $D_p$  was less than about 300 nm, the uncertainty varied from 14% to 24% with a mean value of 22 %, indicating large  
209 uncertainty in  $\text{BCMSD}_{\text{AAC-AE33}}$  for  $D_p$  less than 300 nm.

210 The MAC lookup table was replaced with original  $\overline{\text{MAC}}$  minus its std (-stdMAC) and plus its std (+stdMAC). The resulting  
211 MAC lookup tables were taken into the method proposed by Zhao et al. (2021), and applied to the entire measurement period to  
212 study the influence of MAC variation on the  $\text{BCMSD}_{\text{AAC-AE33}}$ .  $\overline{\text{BCMSD}}_{\text{AAC-AE33}}$  and mean  $\text{BCMSD}_{\text{AAC-AE33}}$  of  $\pm\text{stdMAC}$  were  
213 shown in Fig. 4a. The uncertainty increased with decreasing  $D_p$ , and reached to maximum when  $D_p$  was less than 300 nm,  
214 indicating the  $\text{BCMSD}_{\text{AAC-AE33}}$  for  $D_p$  less than 300 nm might potentially have nonnegligible uncertainty. The uncertainty in bulk  
215  $m_{\text{BC}}$  was from -20 % (+stdMAC) to +28 % (-stdMAC), which was the largest among the four uncertainty sources, as shown in  
216 Table 1.

#### 217 4.2 Uncertainty from the transfer function inversion

218 As stated in Sect. 2.4.1, correction for particle loss and spectral broadening was required when  $\sigma_{\text{ab,binned}}$  was converted to



219  $\sigma_{\text{ab,size-resolved}}$ .  $\lambda_{\Omega}$  was defined to correct particle loss where  $\lambda_{\Omega} = 0$  ( $\lambda_{\Omega} = 1$ ) stood for total (no) particle loss. The relationships  
220 between  $\lambda_{\Omega}$  and  $D_p$  as well as  $Q_{\text{sample}}$ , as shown in Fig. S4a, were well developed (Karlsson and Martinsson, 2003) and  
221 consistent with experimental data of AAC (Johnson et al., 2018).  $Q_{\text{sample}}$  used in this study was  $3.0 \text{ L min}^{-1}$ .  $Q_{\text{sample}}$  was changed  
222 from  $-30\%$  ( $2.1 \text{ L min}^{-1}$ ) to  $+30\%$  ( $3.9 \text{ L min}^{-1}$ ), and the resulting  $\lambda_{\Omega}$  was used to study the fluctuation of  $Q_{\text{sample}}$  on  $\lambda_{\Omega}$ . As  
223 shown in Fig. S4a, the variation of  $\lambda_{\Omega}$  was less than  $0.5\%$ , which was negligible.

224 Spectral broadening was caused by small-size particle diffusion as well as fluctuation of sheath flow and described by  $\mu_{\Omega}$  where  
225  $\mu_{\Omega} < 1$  ( $\mu_{\Omega} = 1$ ) was for (no) broadening.  $\mu_{\Omega}$  was parameterized because of the complicated fluid dynamics and its interaction  
226 with particles. Johnson et al. (2018) parameterized  $\mu_{\Omega}$  based on  $R_t = 10$  (Fig. S4b). However,  $R_t$  was about  $2.5$  in this study,  
227 which might lead to uncertainty.  $\mu_{\Omega}$  was varied from  $-23\%$  to  $+30\%$  to study the impact of  $\mu_{\Omega}$  on  $\text{BCMSD}_{\text{AAC-AE33}}$ . The reason  
228 for the lower limit of  $\mu_{\Omega}$  set as  $-23\%$  rather than  $-30\%$  was that  $\text{BCMSD}_{\text{AAC-AE33}}$  was negative when  $\mu_{\Omega}$  was less than  $-23\%$ .  
229 The resulting influence on the  $\text{BCMSD}_{\text{AAC-AE33}}$  was shown in Fig. 4b. The uncertainty of  $\mu_{\Omega}$  did not exhibit a significant size  
230 dependence. Lower  $\mu_{\Omega}$  led to lower  $\text{BCMSD}_{\text{AAC-AE33}}$ , and vice versa. It should be noted that the uncertainty in the  $m_{\text{BC,bulk}}$  was  
231 from  $-1\%$  ( $-23\%$  of  $\mu_{\Omega}$ ) to  $+21\%$  ( $+30\%$  of  $\mu_{\Omega}$ ), implying systematic overestimation of  $m_{\text{BC,bulk}}$ . Therefore,  $\mu_{\Omega}$  was replaced  
232 with  $-23\%$  of its original value in this work to offset the bias due to the incomplete  $\mu_{\Omega}$  parameterization.

233  $\sigma_{\text{ab,size-resolved}}$  (Fig. S5b) was integrated and the result, denoted as  $\sigma_{\text{ab,bulk,calc}}$ , was compared to  $\sigma_{\text{ab,bulk}}$ . As shown in Fig.  
234 S5a,  $\sigma_{\text{ab,bulk,calc}}$  was consistent with  $\sigma_{\text{ab,bulk}}$ .  $R^2$ ,  $b_1$  and  $b_0$  between  $\sigma_{\text{ab,bulk,calc}}$  and  $\sigma_{\text{ab,bulk}}$  was  $0.9$ ,  $1.1$ , and  $0.5 \text{ Mm}^{-1}$   
235 (Fig. S6), respectively, which validated conversion from  $\sigma_{\text{ab,binned}}$  to  $\sigma_{\text{ab,size-resolved}}$ .

#### 236 4.3 Uncertainty from number fraction of BC-containing particle

237 BC-containing aerosol particles had complicated mixing states. Even for internally-mixed particles with same  $D_p$ , the internal  
238 BC cores might have different  $D_c$ , which could not be resolved by AAC – AE33. Field measurement (Liu et al., 2010) revealed that  
239  $f_{\text{BC}}$  varied with time,  $D_c$  and  $D_p$ . This complexity was simplified to a parameterized fixed value of  $f_{\text{BC}}$  in this study. A fixed  $f_{\text{BC}}$   
240 implied that only one  $D_c$  value corresponded to a given  $D_p$  and the size-resolved number concentration of BC-containing particle  
241 was determined by  $N_{\text{size-resolved}}$  times  $f_{\text{BC}}$ . Zhao et al. (2021) used  $f_{\text{BC}}$  value of  $0.17$  based on SP2 measurement. However,  
242 SP2-derived  $f_{\text{BC}}$  could not represent the bulk  $f_{\text{BC}}$  over the whole particle size spectrum due to the detection limit of SP2. And  
243 different regions might have different  $f_{\text{BC}}$ . In this study,  $f_{\text{BC}}$  was varied and the resulting  $m_{\text{BC,bulk,AAC-AE33,part}}$  was compared  
244 with  $m_{\text{BC,bulk,DMA-SP2}}$ .  $f_{\text{BC}}$  was set as  $0.35$  in this study because  $b_1$  was  $1.0$  between  $m_{\text{BC,bulk,AAC-AE33,part}}$  and  
245  $m_{\text{BC,bulk,DMA-SP2}}$  when  $f_{\text{BC}}$  was  $0.35$ .

246  $f_{\text{BC}}$  was varied from  $0.25$  ( $-30\%$  of  $0.35$ ) to  $0.46$  ( $+30\%$  of  $0.35$ ) to analyze the influence of  $f_{\text{BC}}$  on the  $\text{BCMSD}_{\text{AAC-AE33}}$ , as  
247 shown in Fig. 4c.  $\text{BCMSD}_{\text{AAC-AE33}}$  was more influenced around  $870 \text{ nm}$ . The variation of  $f_{\text{BC}}$  led to uncertainty of  $\pm 3\%$  in  
248  $m_{\text{BC,bulk}}$ , indicating that simplification of  $f_{\text{BC}}$  was a minor uncertainty source compared to MAC and transfer function inversion.

#### 249 4.4 Uncertainty from instrumental noise

250 The instrumental noise stemmed from the fluctuation of the light source and flow of AE33, which was reflected as fluctuation in





251  $I$ ,  $I_0$  and  $F$ , further leading to the fluctuation in ATN,  $\sigma_{\text{ATN}}$  and  $\sigma_{\text{ab}}$ . The instrumental noise was defined as the std of  $\sigma_{\text{ab,binned}}$   
252 and was shown in Fig. S7b. It could be seen that the instrumental noise did not exhibit significant dependence on  $D_p$ . Comparing  
253 Fig. S7a and Fig. S7b, the instrumental noise was irrelevant to the value of  $\sigma_{\text{ab,binned}}$ . Figure S7c illustrated that the instrumental  
254 noise was also not correlated to  $\sigma_{\text{ab,bulk}}$ , implying that the instrumental noise was not dependent on the pollution level.

255 The std of instrumental noise was added to (subtracted from)  $\sigma_{\text{ab,binned}}$  and the derived  $\text{BCMSD}_{\text{AAC-AE33}}$  was used to study the  
256 influence of instrumental noise on  $\text{BCMSD}_{\text{AAC-AE33}}$ . The mean result was shown in Fig. 4d.  $\text{BCMSD}_{\text{AAC-AE33}}$  larger than 1000  
257 nm was more influenced by the instrumental noise than  $\text{BCMSD}_{\text{AAC-AE33}}$  smaller than 500 nm.  $\sigma_{\text{ab,binned}}$  larger than 1000 nm  
258 was relatively small (about  $0.3 \text{ Mm}^{-1}$ ) compared to  $\sigma_{\text{ab,binned}}$  less than 870 nm (about  $0.9 \text{ Mm}^{-1}$ ). The mean instrumental noise was  
259  $0.1 \text{ Mm}^{-1}$  and exhibited no significant dependence on  $D_p$ . Therefore,  $\sigma_{\text{ab,binned}}$  larger than 1000 nm was more affected by the  
260 instrumental noise, resulting in distinct variation in  $\text{BCMSD}_{\text{AAC-AE33}}$ . Since the mass fraction of  $m_{\text{BC,bulk}}$  was not dominated by  
261  $\text{BCMSD}$  larger than 1000 nm in this study, the resulting uncertainty in  $m_{\text{BC,bulk}}$  was not obvious, which varied from  $-2\%$  to  $-$   
262  $1\%$ , also minor compared to MAC and transfer function inversion.

## 263 5 Conclusions

264 Knowledge of bulk black carbon (BC) characteristics, such as bulk BC mass concentration ( $m_{\text{BC,bulk}}$ ), was very limited for deeper  
265 understanding the influence of BC on radiation and health. BC mass size distribution (BCMSD) was one of the BC microphysical  
266 characteristics that could indicate emission source, reflect atmospheric aging and effectively reduce uncertainty related to BC  
267 radiative effect. However, current BCMSD measurement ranging from upper micron to larger than  $1 \mu\text{m}$  was insufficient in time  
268 resolution and sophisticated for routine measurement. In this study, a new method to determine BCMSD was proposed characterized  
269 by wide size range of measurement up to  $1.5 \mu\text{m}$ , high time resolution up to 1 hour and convenience for extensive measurement.  
270 The BCMSD was retrieved by size-resolved absorption coefficient ( $\sigma_{\text{ab,size-resolved}}$ ) measured by an aerodynamic aerosol classifier  
271 in tandem with an aethalometer model AE33 (AAC – AE33), denoted as  $\text{BCMSD}_{\text{AAC-AE33}}$ . Size-resolved number concentration  
272 ( $N_{\text{size-resolved}}$ ) was measured concurrently by scanning mobility particle sizer (SMPS) and an aerodynamic particle sizer (APS) to  
273 model the influence of size on mass absorption cross-section (MAC).

274 The proposed method was applied to a field measurement in Yangtze River Delta and validated by comparing the BCMSD with  
275 that measured by an differential mobility analyzer in tandem with a single-particle soot photometer (DMA – SP2), denoted as  
276  $\text{BCMSD}_{\text{DMA-SP2}}$ . The results showed that for particle diameter ( $D_p$ ) less than 300 nm,  $\text{BCMSD}_{\text{AAC-AE33}}$  was higher than  
277  $\text{BCMSD}_{\text{DMA-SP2}}$ , which might be caused by underestimated MAC by the method proposed by Zhao et al. (2021) or incomplete  
278 parameterization of spectral broadening of AAC.  $\text{BCMSD}_{\text{AAC-AE33}}$  was consistent with  $\text{BCMSD}_{\text{DMA-SP2}}$  for  $D_p$  larger than 300  
279 nm.  $m_{\text{BC,bulk}}$  integrated over the size range that AAC – AE33 and DMA – SP2 both measured, denoted as  $m_{\text{BC,bulk,AAC-AE33,part}}$   
280 and  $m_{\text{BC,bulk,DMA-SP2}}$ , compared well with each other with determination coefficient ( $R^2$ ), slope ( $b_1$ ), and intercept ( $b_0$ ) of 0.8, 1.0  
281 and  $0.1 \mu\text{g m}^{-3}$ , respectively. However, DMA – SP2 could not measure  $D_p$  larger than 700 nm, leading to  $0.2 \mu\text{g m}^{-3}$  (33 %)   
282 underestimation of  $m_{\text{BC,bulk}}$ , highlighting the necessity to measure BCMSD with a wider size range.



283 Uncertainty analysis was performed with respect to MAC, transfer function inversion, number fraction of BC-containing ( $f_{BC}$ )  
284 and instrumental noise. MAC was the largest uncertainty source, leading to significant uncertainty for  $D_p$  less than 300 nm and  
285 about 24% uncertainty in  $m_{BC,bulk}$ . Transfer function inversion was the second largest uncertainty source, which was induced by  
286 incomplete parameterization of spectral broadening. The uncertainty in transfer function inversion led to systematic overestimation  
287 of  $m_{BC,bulk}$ , which was corrected in this study. Both  $f_{BC}$  and instrumental noise were minor uncertainty sources and one order of  
288 magnitude less than MAC and transfer function inversion.  $f_{BC}$  was simplification of complicated BC mixing states, leading to  
289 relatively big uncertainty in BCMSD at 870 nm, around the boundary between condensation mode and droplet mode. The BCMSD  
290 for  $D_p$  larger than 1000 nm was more sensitive to instrumental noise.

291 This study proposed a new method to determine BCMSD based on widespread filter-based measurement. The proposed method  
292 was validated by well-designed field measurement and thorough uncertainty analysis, highlighting the necessity to measure BCMSD  
293 with a wider size coverage for a more complete characterization of BCMSD. The new method provided a high-time-resolution,  
294 wide-size-coverage, convenient and cost-effective solution for BCMSD measurement. Hence, the proposed method had great  
295 potential for widespread BCMSD measurement and was expected to promote the research of BC radiative effect, source  
296 apportionment and atmospheric aging.

#### 297 **Data availability**

298 The measurement data involved in this study are available upon request to the authors.

#### 299 **Author contributions**

300 CZ determined the main goal of this study. WZ and GZ designed the methods. WZ carried them out and prepared the paper with  
301 contributions from all co-authors.

#### 302 **Competing interests**

303 The authors declare that they have no conflict of interest.

#### 304 **References**

- 305 Bond, T. C.: Spectral dependence of visible light absorption by carbonaceous particles emitted from coal combustion, *Geophys. Res.*  
306 *Letts.*, 28, 4075-4078, 10.1029/2001gl013652, 2001.
- 307 Bond, T. C., Streets, D. G., Yarber, K. F., Nelson, S. M., Woo, J. H., and Klimont, Z.: A technology-based global inventory of black  
308 and organic carbon emissions from combustion, *J. Geophys. Res.-Atmos.*, 109, 43, 10.1029/2003jd003697, 2004.
- 309 Bond, T. C., and Bergstrom, R. W.: Light absorption by carbonaceous particles: An investigative review, *Aerosol Science and*  
310 *Technology*, 40, 27-67, 10.1080/02786820500421521, 2006.
- 311 Bond, T. C., Doherty, S. J., Fahey, D. W., Forster, P. M., Berntsen, T., DeAngelo, B. J., Flanner, M. G., Ghan, S., Karcher, B., Koch,  
312 D., Kinne, S., Kondo, Y., Quinn, P. K., Sarofim, M. C., Schultz, M. G., Schulz, M., Venkataraman, C., Zhang, H., Zhang, S., Bellouin,  
313 N., Guttikunda, S. K., Hopke, P. K., Jacobson, M. Z., Kaiser, J. W., Klimont, Z., Lohmann, U., Schwarz, J. P., Shindell, D., Storelvmo,  
314 T., Warren, S. G., and Zender, C. S.: Bounding the role of black carbon in the climate system: A scientific assessment, *J. Geophys.*



- 315 Res.-Atmos., 118, 5380-5552, 10.1002/jgrd.50171, 2013.
- 316 Castagna, J., Calvello, M., Esposito, F., and Pavese, G.: Analysis of equivalent black carbon multi-year data at an oil pre-treatment  
317 plant: Integration with satellite data to identify black carbon transboundary sources, *Remote Sens. Environ.*, 235, 10,  
318 10.1016/j.rse.2019.111429, 2019.
- 319 Chow, J. C., Watson, J. G., Crow, D., Lowenthal, D. H., and Merrifield, T.: Comparison of IMPROVE and NIOSH Carbon  
320 Measurements, *Aerosol Science and Technology*, 34, 23-34, 10.1080/02786820119073, 2001.
- 321 DeCarlo, P. F., Slowik, J. G., Worsnop, D. R., Davidovits, P., and Jimenez, J. L.: Particle morphology and density characterization  
322 by combined mobility and aerodynamic diameter measurements. Part 1: Theory (vol 38, pg 1185, 2004), *Aerosol Science and*  
323 *Technology*, 39, 184-184, 10.1080/02786820590928897, 2005.
- 324 Drinovec, L., Mocnik, G., Zotter, P., Prevot, A. S. H., Ruckstuhl, C., Coz, E., Rupakheti, M., Sciare, J., Muller, T., Wiedensohler,  
325 A., and Hansen, A. D. A.: The "dual-spot" Aethalometer: an improved measurement of aerosol black carbon with real-time loading  
326 compensation, *Atmospheric Measurement Techniques*, 8, 1965-1979, 10.5194/amt-8-1965-2015, 2015.
- 327 Guo, Y. H.: Carbonaceous aerosol composition over northern China in spring 2012, *Environmental Science and Pollution Research*,  
328 22, 10839-10849, 10.1007/s11356-015-4299-8, 2015.
- 329 Hansen, A. D. A., Rosen, H., and Novakov, T.: The aethalometer - an instrument for the real-time measurement of optical-absorption  
330 by aerosol-particles, *Sci. Total Environ.*, 36, 191-196, 10.1016/0048-9697(84)90265-1, 1984.
- 331 Helin, A., Niemi, J. V., Virkkula, A., Pirjola, L., Teinila, K., Backman, J., Aurela, M., Saarikoski, S., Ronkko, T., Asmi, E., and  
332 Timonen, H.: Characteristics and source apportionment of black carbon in the Helsinki metropolitan area, Finland, *Atmospheric*  
333 *Environment*, 190, 87-98, 10.1016/j.atmosenv.2018.07.022, 2018.
- 334 Highwood, E. J., and Kinnarsley, R. P.: When smoke gets in our eyes: The multiple impacts of atmospheric black carbon on climate,  
335 air quality and health, *Environment International*, 32, 560-566, 10.1016/j.envint.2005.12.003, 2006.
- 336 Johnson, T. J., Irwin, M., Symonds, J. P. R., Olfert, J. S., and Boies, A. M.: Measuring aerosol size distributions with the aerodynamic  
337 aerosol classifier, *Aerosol Science and Technology*, 52, 655-665, 10.1080/02786826.2018.1440063, 2018.
- 338 Karlsson, M. N. A., and Martinsson, B. G.: Methods to measure and predict the transfer function size dependence of individual  
339 DMAs, *Journal of Aerosol Science*, 34, 603-625, 10.1016/s0021-8502(03)00020-x, 2003.
- 340 Kim, J. H., Mulholland, G. W., Kukuck, S. R., and Pui, D. Y. H.: Slip correction measurements of certified PSL nanoparticles using  
341 a nanometer differential mobility analyzer (nano-DMA) for Knudsen number from 0.5 to 83, *J. Res. Natl. Inst. Stand. Technol.*, 110,  
342 31-54, 10.6028/jres.110.005, 2005.
- 343 Liu, C., Chung, C. E., Yin, Y., and Schnaiter, M.: The absorption Angstrom exponent of black carbon: from numerical aspects,  
344 *Atmospheric Chemistry and Physics*, 18, 6259-6273, 10.5194/acp-18-6259-2018, 2018.
- 345 Liu, D., Flynn, M., Gysel, M., Targino, A., Crawford, I., Bower, K., Choularton, T., Juranyi, Z., Steinbacher, M., Huglin, C., Curtius,  
346 J., Kampus, M., Petzold, A., Weingartner, E., Baltensperger, U., and Coe, H.: Single particle characterization of black carbon



347 aerosols at a tropospheric alpine site in Switzerland, *Atmospheric Chemistry and Physics*, 10, 7389-7407, 10.5194/acp-10-7389-  
348 2010, 2010.

349 Matsui, H., Hamilton, D. S., and Mahowald, N. M.: Black carbon radiative effects highly sensitive to emitted particle size when  
350 resolving mixing-state diversity, *Nature Communications*, 9, 10.1038/s41467-018-05635-1, 2018.

351 Moosmuller, H., Chakrabarty, R. K., and Arnott, W. P.: Aerosol light absorption and its measurement: A review, *Journal of*  
352 *Quantitative Spectroscopy & Radiative Transfer*, 110, 844-878, 10.1016/j.jqsrt.2009.02.035, 2009.

353 Ning, Z., Chan, K. L., Wong, K. C., Westerdahl, D., Mocnik, G., Zhou, J. H., and Cheung, C. S.: Black carbon mass size distributions  
354 of diesel exhaust and urban aerosols measured using differential mobility analyzer in tandem with Aethalometer, *Atmospheric*  
355 *Environment*, 80, 31-40, 10.1016/j.atmosenv.2013.07.037, 2013.

356 Onasch, T. B., Trimborn, A., Fortner, E. C., Jayne, J. T., Kok, G. L., Williams, L. R., Davidovits, P., and Worsnop, D. R.: Soot  
357 Particle Aerosol Mass Spectrometer: Development, Validation, and Initial Application, *Aerosol Science and Technology*, 46, 804-  
358 817, 10.1080/02786826.2012.663948, 2012.

359 Ramachandran, S., and Rajesh, T. A.: Black carbon aerosol mass concentrations over Ahmedabad, an urban location in western  
360 India: Comparison with urban sites in Asia, Europe, Canada, and the United States, *J. Geophys. Res.-Atmos.*, 112, 19,  
361 10.1029/2006jd007488, 2007.

362 Ran, L., Deng, Z. Z., Wang, P. C., and Xia, X. A.: Black carbon and wavelength-dependent aerosol absorption in the North China  
363 Plain based on two-year aethalometer measurements, *Atmospheric Environment*, 142, 132-144, 10.1016/j.atmosenv.2016.07.014,  
364 2016.

365 Schwarz, J. P., Gao, R. S., Fahey, D. W., Thomson, D. S., Watts, L. A., Wilson, J. C., Reeves, J. M., Darbeheshti, M., Baumgardner,  
366 D. G., Kok, G. L., Chung, S. H., Schulz, M., Hendricks, J., Lauer, A., Karcher, B., Slowik, J. G., Rosenlof, K. H., Thompson, T. L.,  
367 Langford, A. O., Loewenstein, M., and Aikin, K. C.: Single-particle measurements of midlatitude black carbon and light-scattering  
368 aerosols from the boundary layer to the lower stratosphere, *J. Geophys. Res.-Atmos.*, 111, 15, 10.1029/2006jd007076, 2006.

369 Schwarz, J. P., Spackman, J. R., Fahey, D. W., Gao, R. S., Lohmann, U., Stier, P., Watts, L. A., Thomson, D. S., Lack, D. A., Pfister,  
370 L., Mahoney, M. J., Baumgardner, D., Wilson, J. C., and Reeves, J. M.: Coatings and their enhancement of black carbon light  
371 absorption in the tropical atmosphere, *J. Geophys. Res.-Atmos.*, 113, 10, 10.1029/2007jd009042, 2008.

372 Soto-Garcia, L. L., Andreae, M. O., Andreae, T. W., Artaxo, P., Maenhaut, W., Kirchstetter, T., Novakov, T., Chow, J. C., and Mayol-  
373 Bracero, O. L.: Evaluation of the carbon content of aerosols from the burning of biomass in the Brazilian Amazon using thermal,  
374 optical and thermal-optical analysis methods, *Atmospheric Chemistry and Physics*, 11, 4425-4444, 10.5194/acp-11-4425-2011, 2011.

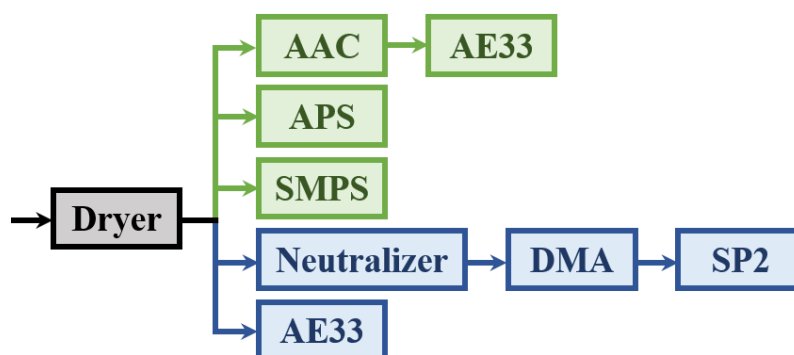
375 Tavakoli, F., and Olfert, J. S.: An Instrument for the Classification of Aerosols by Particle Relaxation Time: Theoretical Models of  
376 the Aerodynamic Aerosol Classifier, *Aerosol Science and Technology*, 47, 916-926, 10.1080/02786826.2013.802761, 2013.

377 Tunved, P., Cremer, R. S., Zieger, P., and Strom, J.: Using correlations between observed equivalent black carbon and aerosol size  
378 distribution to derive size resolved BC mass concentration: a method applied on long-term observations performed at Zeppelin



379 station, Ny-Alesund, Svalbard, Tellus Ser. B-Chem. Phys. Meteorol., 73, 1-17, 10.1080/16000889.2021.1933775, 2021.  
380 Viidanoja, J., Kerminen, V.-M., and Hillamo, R.: Measuring the Size Distribution of Atmospheric Organic and Black Carbon Using  
381 Impactor Sampling Coupled with Thermal Carbon Analysis: Method Development and Uncertainties, Aerosol Science and  
382 Technology, 36, 607-616, 10.1080/02786820252883847, 2002.  
383 Yu, H., Wu, C., Wu, D., and Yu, J. Z.: Size distributions of elemental carbon and its contribution to light extinction in urban and  
384 rural locations in the pearl river delta region, China, Atmospheric Chemistry and Physics, 10, 5107-5119, 10.5194/acp-10-5107-  
385 2010, 2010.  
386 Zhang, R. Y., Khalizov, A. F., Pagels, J., Zhang, D., Xue, H. X., and McMurry, P. H.: Variability in morphology, hygroscopicity, and  
387 optical properties of soot aerosols during atmospheric processing, Proceedings of the National Academy of Sciences of the United  
388 States of America, 105, 10291-10296, 10.1073/pnas.0804860105, 2008.  
389 Zhao, G., Tao, J. C., Kuang, Y., Shen, C. Y., Yu, Y. L., and Zhao, C. S.: Role of black carbon mass size distribution in the direct  
390 aerosol radiative forcing, Atmospheric Chemistry and Physics, 19, 13175-13188, 10.5194/acp-19-13175-2019, 2019.  
391 Zhao, G., Shen, C. Y., and Zhao, C. S.: Technical note: Mismeasurement of the core-shell structure of black carbon-containing  
392 ambient aerosols by SP2 measurements, Atmospheric Environment, 243, 10.1016/j.atmosenv.2020.117885, 2020a.  
393 Zhao, G., Yu, Y., Tian, P., Li, J., Guo, S., and Zhao, C.: Evaluation and Correction of the Ambient Particle Spectral Light Absorption  
394 Measured Using a Filter-based Aethalometer, Aerosol and Air Quality Research, 20, 10.4209/aaqr.2019.10.0500, 2020b.  
395 Zhao, W. L., Tan, W. S., Zhao, G., Shen, C. Y., Yu, Y. L., and Zhao, C. S.: Determination of equivalent black carbon mass  
396 concentration from aerosol light absorption using variable mass absorption cross section, Atmospheric Measurement Techniques,  
397 14, 1319-1331, 10.5194/amt-14-1319-2021, 2021.

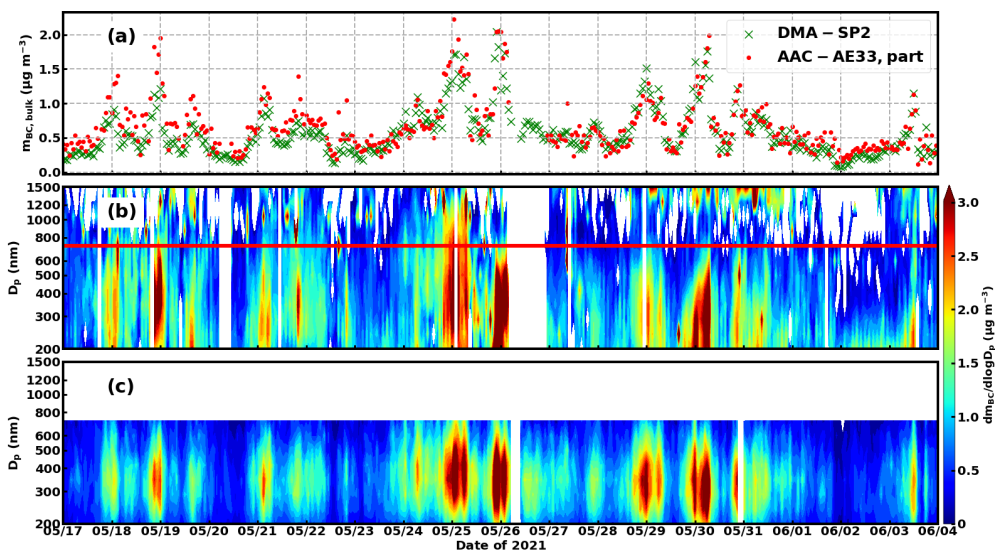
398



399

400 **Figure 1: Schematic diagram of the measurement (green) and the validation (blue) setup.**

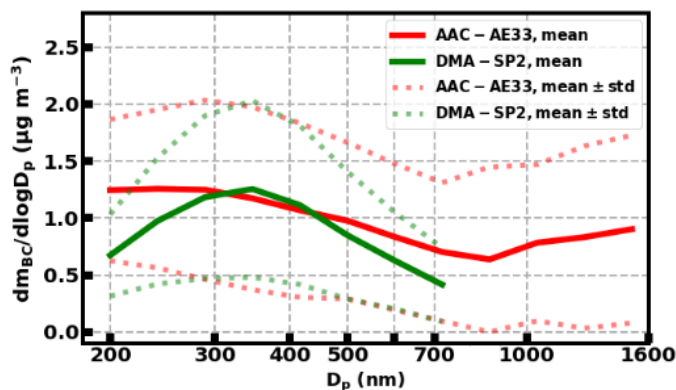
401



402

403 Figure 2: Time series of (a)  $m_{BC,bulk}$  from BCMSD integrated from 200 nm to 720 nm determined by the proposed method  
 404 (red dot, denoted as AAC – AE33, part) and DMA – SP2 (green cross, denoted as DMA – SP2), BCMSD determined by (b)  
 405 the proposed method and (c) DMA – SP2. The red line in (b) marked particle size of 720 nm.

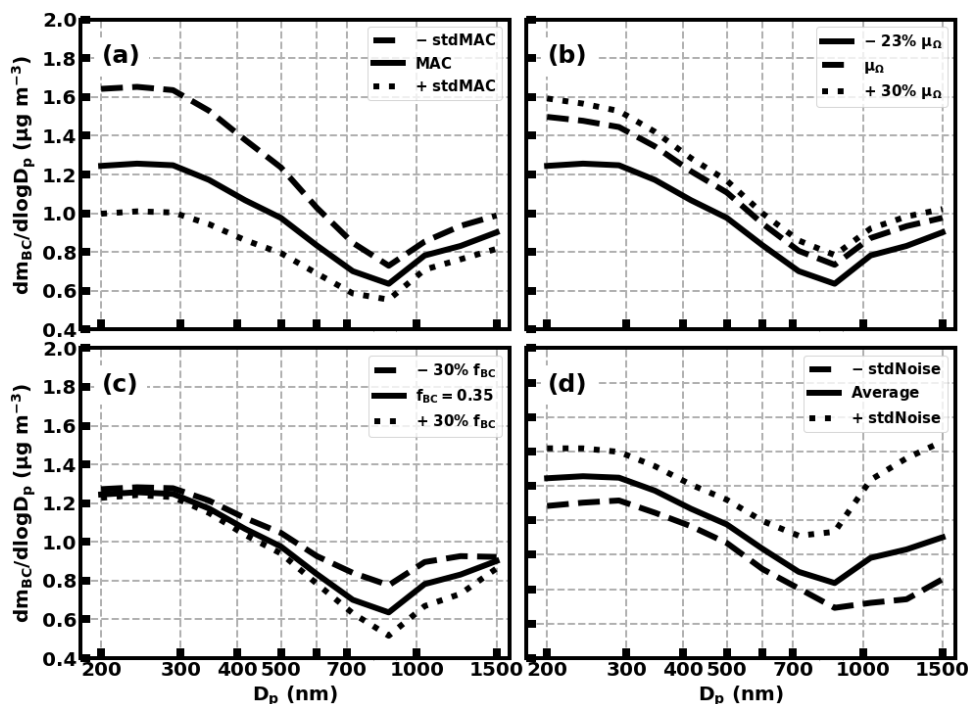
406



407

408 Figure 3: Mean and std of  $BCMSD_{AAC-AE33}$  (green) and  $BCMSD_{DMA-SP2}$  (red) during the measurement period. Mean  
 409  $BCMSD$  was denoted by the solid line. Mean  $\pm$  std of  $BCMSD$  was denoted by the dotted line.

410



411  
 412 **Figure 4:** Uncertainty in  $\text{BCMSD}_{\text{AAC-AE33}}$  arising from (a) MAC lookup table, (b) transfer function inversion, (c)  $f_{\text{BC}}$  and  
 413 (d) instrumental noise. The solid lines in each panel were the same and are mean  $\text{BCMSD}_{\text{AAC-AE33}}$  during the measurement  
 414 period. The dotted lines and dashed lines in each panel were mean  $\text{BCMSD}_{\text{AAC-AE33}} \pm$  standard deviation (std) calculated  
 415 from (a) MAC + std of MAC and MAC – std of MAC, (b) default  $\mu_{\Omega}$  and 1.3 times default  $\mu_{\Omega}$ , (c)  $f_{\text{BC}}$  of 35% times 0.7  
 416 and 1.3, (d)  $\text{BCMSD}_{\text{AAC-AE33}} +$  std of instrumental noise and – std of instrumental noise.

417

418 **Table 1:** The Uncertainty in the bulk  $m_{\text{BC}}$  resulted from MAC lookup table, transfer function inversion,  $f_{\text{BC}}$  and  
 419 instrumental noise.

Uncertainty source	MAC	Transfer function inversion	$f_{\text{BC}}$	Instrumental noise
Uncertainty in $m_{\text{BC,bulk}}$	– 20 % ~ + 28 %	– 1 % ~ + 21 %	– 3 % ~ + 3 %	– 2 % ~ – 1 %

420